A parametric study of axial flow jets for mitigation of vortex rope instabilities

Citation for the original published paper (version of record):
Salehi, S., Nilsson, H. (2025). A parametric study of axial flow jets for mitigation of vortex rope instabilities. 10TH IAHR WORKGROUP MEETING ON CAVITATION AND DYNAMIC PROBLEMS IN HYDRAULIC MACHINERY AND SYSTEMS, 1561.
http://dx.doi.org/10.1088/1755-1315/1561/1/012023

IOP Conference Series:
Earth and
Environmental Science

PAPER • **OPEN ACCESS**

A parametric study of axial flow jets for mitigation of vortex rope instabilities

To cite this article: Saeed Salehi and Håkan Nilsson 2025 *IOP Conf. Ser.: Earth Environ. Sci.* **1561** 012023

IAHRWG2025 IOP Publishing
IOP Conf. Series: Earth and Environmental Science **1561** (2025) 012023 doi:10.1088/1755-1315/1561/1/012023

A parametric study of axial flow jets for mitigation of vortex rope instabilities

Saeed Salehi[a,b], **Håkan Nilsson**[a]

[a] Division of Fluid Dynamics, Department of Mechanics and Maritime Sciences, Chalmers University of Technology, SE-412 96 Gothenburg, Sweden
[b] Division of Applied Thermodynamics and Fluid Mechanics, Department of Management and Engineering, Linköping University, SE-581 83 Linköping, Sweden

E-mail: `saeed.salehi@liu.se`

Abstract.
Hydraulic turbines are typically designed to operate continuously at their optimal efficiency. However, the growing reliance on intermittent energy sources has resulted in more frequent operation under transient and off-design conditions, which increases stress on the turbines and shortens their lifespan. Swirling flow deceleration in the draft tube of hydraulic turbines operating at part load often triggers a self-excited instability known as the vortex rope. This phenomenon generates significant pressure fluctuations that may compromise the structural durability of the turbine. Therefore, it is crucially important to study and mitigate such instabilities. The current work presents a detailed study of the impact of axial flow jets on the vortex rope instability in hydraulic turbines, particularly under Part Load (PL) conditions. Utilizing the Timisoara Swirl Generator (TSG) model, we conducted a comprehensive parametric study to analyze the effects of axial water injection through the runner hub on mitigating vortex rope instabilities. The numerical simulations are performed using the open-source CFD code OpenFOAM. The results indicate that increasing the jet flow rate moves the vortex rope and stagnant region downstream, significantly reducing pressure pulsations and hydrodynamic instabilities. The study identifies a critical jet flow rate at which the vortex rope diminishes, enhancing turbine performance and operational flexibility. The current parametric study can be considered a first step toward achieving the optimal strategy for active flow control of self-induced instabilities within hydraulic turbines.

1. Introduction

The rapid growth of renewable energy sources, like solar and wind, addresses global energy demand, but their intermittent nature requires integration with controllable sources. Hydropower systems play a key role in ensuring grid flexibility and energy storage, owing to their high reliability and rapid response across a range of time scales [1].

While hydraulic turbines were initially developed for steady operation at the Best Efficiency Point (BEP), their role has expanded to include frequent off-design and transient operation to assist in grid stabilization. These off-design operations result in residual angular momentum at the runner exit, leading to decelerating swirling flows in the draft tube that can cause vortex breakdown and hydrodynamic instabilities. One notable instability is the vortex rope, which occurs at Part Load (PL) conditions in hydraulic turbines.

The vortex rope phenomenon is a self-induced instability in hydropower systems, resulting in significant pressure pulsations. If these pulsations coincide with the system's natural frequencies, they can cause severe structural vibrations, leading to fatigue damage and a shortened turbine lifespan, with substantial economic repercussions [2]. Therefore, it is essential to develop flow control strategies to mitigate these instabilities, thereby improving the operational flexibility and lifetime of turbines.

Axial water injection through the runner crown has been proposed as an effective way for active flow control and mitigation of the vortex rope [3]. In this article, an in-depth parametric study is performed to further study and explain different physical aspects of the axial jet impact on the vortex rope.

2. Case study

The Timisoara Swirl Generator (TSG) is considered for the investigation in the present work. The machine was designed to investigate self-induced instabilities under adverse pressure gradients [4, 5], which commonly occur under part load conditions in hydraulic turbines. The full TSG model is composed of four components, leaned struts, guide vanes, a runner, and a convergent-divergent pipe. The guide vanes direct the flow toward the runner at a proper angle of attack. The axial runner features 10 blades with a primary function of redistributing the total pressure by increasing the axial velocity near the shroud while simultaneously reducing it near the hub [5]. The runner rotates with the rotational speed of 920 rpm. More information about the test case and its full 3D representation is presented by Ref. [6].

In the current work, a reduced model of TSG including only the convergent-divergent pipe downstream the runner is considered, as sketched in Fig. 1. The setup features a conical test section with a cone angle of $2 \times 8.6^\circ = 17.2^\circ$. The test section is similar to the discharge cone found in Francis turbines and serves as the primary focus for the experimental measurements of the TSG model. MG0 − MG3 denote the positions where the experimental pressure sensors are installed. Here, we used probes on the opposite sides of each position, close to the wall, to perform the plunging and rotating analysis. The active flow control studied in the present work is imposed as a jet below the runner hub.

To mimic the effect of upstream components, the inlet boundary condition was derived from a separate simulation of the full TSG model, including the runner, guide vanes, and struts. The time-averaged velocity components and turbulence quantities (k and ω) recorded at the inlet surface of the convergent–divergent section were then applied in the present simulations using the `timeVaryingMappedFixedValue` boundary condition in OpenFOAM. The main flow rate is considered as $Q = 30$ l/s, while the jet flow rate is varied between 0% to 15% of the main flow rate, i.e. $Q_{\mathrm{jet}}/Q = 0$–15%.

3. Computational aspects

The Unsteady Reynolds-Averaged Navier-Stokes (URANS) equations describe the transient incompressible turbulent flow. The equations require turbulence modeling to account for the unknown Reynolds stress tensor. The Boussinesq (eddy-viscosity) hypothesis, along with the Shear Stress Transport based Scale-Adaptive Simulation model (SST-SAS) [7], is used to calculate the turbulent viscosity (ν_{t}). The SST-SAS is a URANS model frequently utilized for addressing engineering transient flows because of its turbulence-resolving capabilities. The turbulent viscosity is determined by solving the transport equations for turbulent kinetic energy (k) and specific rate of dissipation (ω). Our experiences show that the SST-SAS model can be successfully applied to transient simulations in various hydropower-related applications. [8–11]. The computations are performed using the open-source software OpenFOAM-v2306 [12, 13].

The block-structured mesh used in the study is shown in Fig. 2 and consists of over 2.53 million cells. The computational mesh was selected based on a mesh study including three different meshes, namely, Coarse (7.54×10^5 cells), Medium (1.37×10^6 cells), and Fine (2.53×10^6 cells) and the finest mesh is ultimately chosen for the rest of the study. The results of this mesh study are presented in the next section.

The temporal derivative terms are discretized using the second-order backward implicit scheme. The simulations are marched through time with a fixed time step of $\Delta t = 1.0 \times 10^{-4}$ s. The mean CFL number is kept below 0.25 in all studied cases, while the maximum CFL number does not exceed 20. The convection terms are discretized using the Linear-Upwind Stabilized Transport (LUST) scheme [14], which utilizes a blend of 75% central differencing and 25% second-order upwind differencing.

A spatially non-uniform velocity distribution is imposed at the inlet of the convergent-divergent pipe. The velocity profiles are taken from Ref. [15] which are obtained with 3D computations of the full TSG model. The axial and circumferential velocity profiles, normalized with the test section throat bulk velocity U_t, are illustrated in Fig. 3. The Cartesian velocity components are calculated from these two profiles and applied to the inlet boundary. Additionally, a uniform constant velocity condition is imposed on the jet boundary.

4. Results and discussion

The main purpose of the draft tube in hydraulic turbines is to recover the static pressure. The occurrence of the vortex rope instability generally deteriorates the performance of the draft tubes, leading to a reduction in pressure recovery. The pressure at levels MG0–MG3 (shown in Fig. 1) is monitored throughout the simulations to examine the effectiveness of the flow control mechanism on the pressure recovery of the diverging section. The pressure recovery coefficient (C_p) at different sensor locations is calculated with respect to the MG0 sensor, placed at the

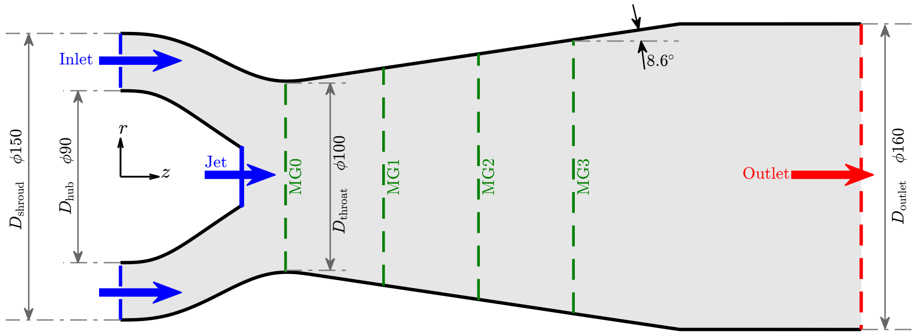

Figure 1: A schematic of the test section of the TSG model that displays geometrical details and locations of pressure sensors MG0, MG1, MG2, and MG3. All dimensions are in mm.

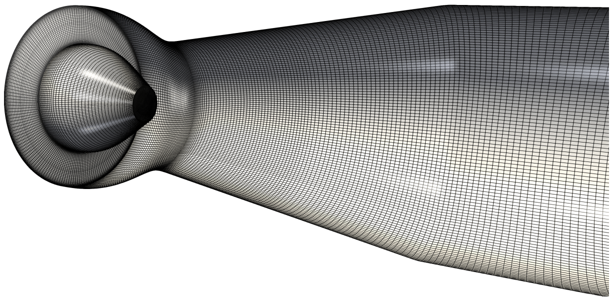

Figure 2: Employed block-structured mesh

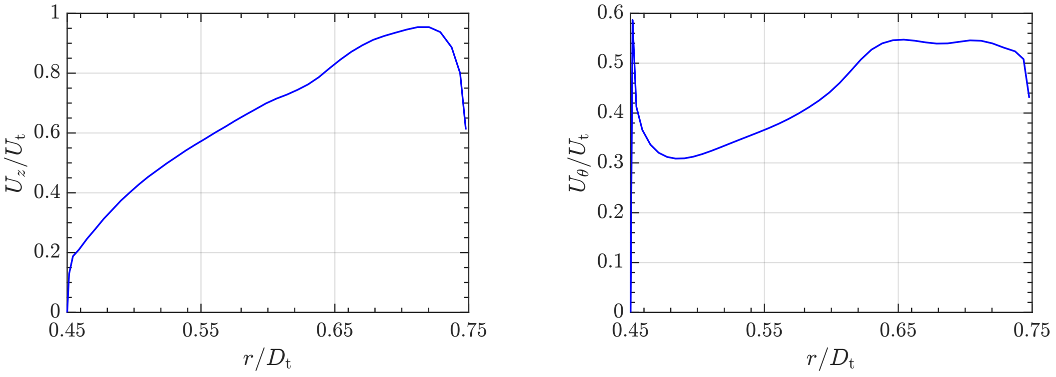

(a) Axial velocity (b) Circumferential velocity

Figure 3: Normalized axial and circumferential velocity profiles imposed at the inlet boundary

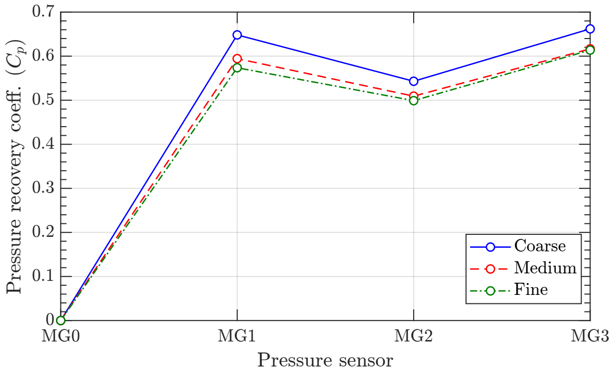

Figure 4: Effect of mesh resolution on the pressure recovery coefficient (C_p) of different sensor locations

throat. Accordingly, C_p reads

$$C_p = \frac{\overline{p} - \overline{p_{\mathrm{MG0}}}}{\frac{1}{2}\rho U_\mathrm{t}^2}, \tag{1}$$

where $\overline{p}$ is the mean pressure, ρ is the density, and U_t is the average velocity at the test section throat.

The pressure recovery is presented in Fig. 4 for the different computational mesh to investigate the effect of mesh resolution on the results. The Medium and Fine mesh show rather similar results, with a maximum relative error of 3.6%. Therefore, the finest mesh with 2.53×10^6 cells is chosen for this parametric study. See Ref. [6] for more detailed verification and validation of the case study.

Fig. 5 demonstrates how the pressure recovery coefficient varies with changes in the jet flow rate percentage, providing insights into the efficiency of pressure recovery under different flow conditions. The pressure recovery is at its lowest when the jet flow rate is zero ($Q_\mathrm{jet}/Q = 0$). As the jet flow rate increases, the pressure recovery coefficient also increases. The most significant increase is observed around $Q_\mathrm{jet}/Q = 10\%$, after which the pressure recovery coefficient becomes less affected by further increasing Q_jet/Q.

It is well-known that the vortex rope typically exhibits two types of oscillations: rotating and plunging [5]. While the vortex rope rotates around the turbine axis, it simultaneously pulsates in the axial direction, a phenomenon known as the plunging effect. The plunging mode is detected throughout the entire machine at the same time, whereas the rotating mode, associated with

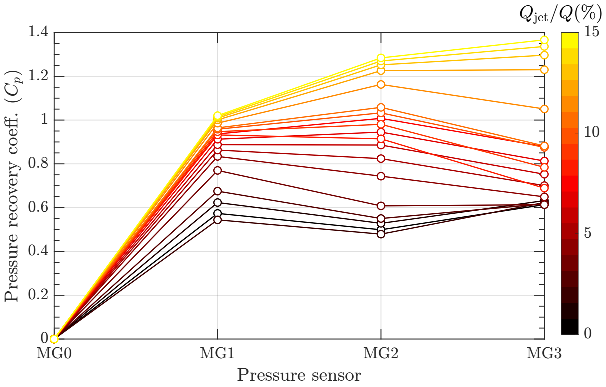

Figure 5: Effect of jet flow rate (Q_{jet}/Q) on the pressure recovery coefficient (C_p) of different sensor locations

the precession of the vortex rope, is active locally within the cross-section. The plunging and rotating effects of the vortex rope are analyzed by decomposing the pressure signals from two opposing probes as

$$\begin{aligned} p_{\mathrm{sync}} &= \frac{p_1 + p_2}{2}, \quad \text{Synchronous (plunging) component,} \\ p_{\mathrm{async}} &= \frac{p_1 - p_2}{2}, \quad \text{Asynchronous (rotating) component.} \end{aligned} \tag{2}$$

In this analysis, p_1 and p_2 denote the pressure signals from two probes located on opposite sides of the same cross-section of the draft tube. p_{sync} refers to the pressure fluctuations detected simultaneously by both probes, representing the plunging mode, whereas p_{async} describes the local pressure variations captured independently by each probe, indicative of the rotating mode.

The pressure decomposition is performed for all four pressure levels (MG0–MG3), and synchronous and asynchronous components are calculated. Subsequently, a Fast Fourier Transform (FFT) analysis is done on the decomposed signals, and the highest amplitude of the pressure fluctuations is extracted. Fig. 6 presents the variation of the highest amplitude of rotating and plunging modes with jet flow rate for different pressure locations.

The amplitude of the rotating mode first decreases for $Q_{\mathrm{jet}}/Q \leq 2\%$. The main reason for this behavior is not yet clear and requires further investigation. A plausible explanation is that the energy is redistributed over multiple modes, while the present analysis considers only the highest-amplitude mode. Therefore, the observed reduction does not necessarily imply that the vortex rope is being removed. After this sudden reduction, the amplitude gradually increases with the jet flow rate. Even though the highest amplitude of the no-jet condition is observed at MG1, for $Q_{\mathrm{jet}}/Q > 2\%$, the MG2 probe exhibits the strongest rotating mode, which indicates that the vortex rope is moving downstream with increasing jet flow rate. The highest amplitude of MG2 is observed at 5% jet flow rate, while the MG3 amplitude continues to grow until $Q_{\mathrm{jet}}/Q = 8.5\%$, denoting further downstream displacement of the vortex rope.

A critical jet flow rate appears to exist, beyond which the rotating mode entirely diminishes, and the amplitude approaches zero. In this study, the critical jet flow rate is observed at $Q_{\mathrm{jet,cr}}/Q = 9.25\%$. This value is slightly lower compared to the experimental findings reported in Ref. [5], which identified the critical jet flow rate at 11.5%.

The plunging mode (bottom plot in Fig. 6) demonstrates a different trend. The amplitude is relatively small at the no-jet condition and increases considerably at $Q_{\mathrm{jet}}/Q = 3\%$, when the vortex rope detaches from the runner hub and moves downstream. However, the plunging mode decreases and diminishes with a further increase in jet flow rate. Unlike the rotating mode, the

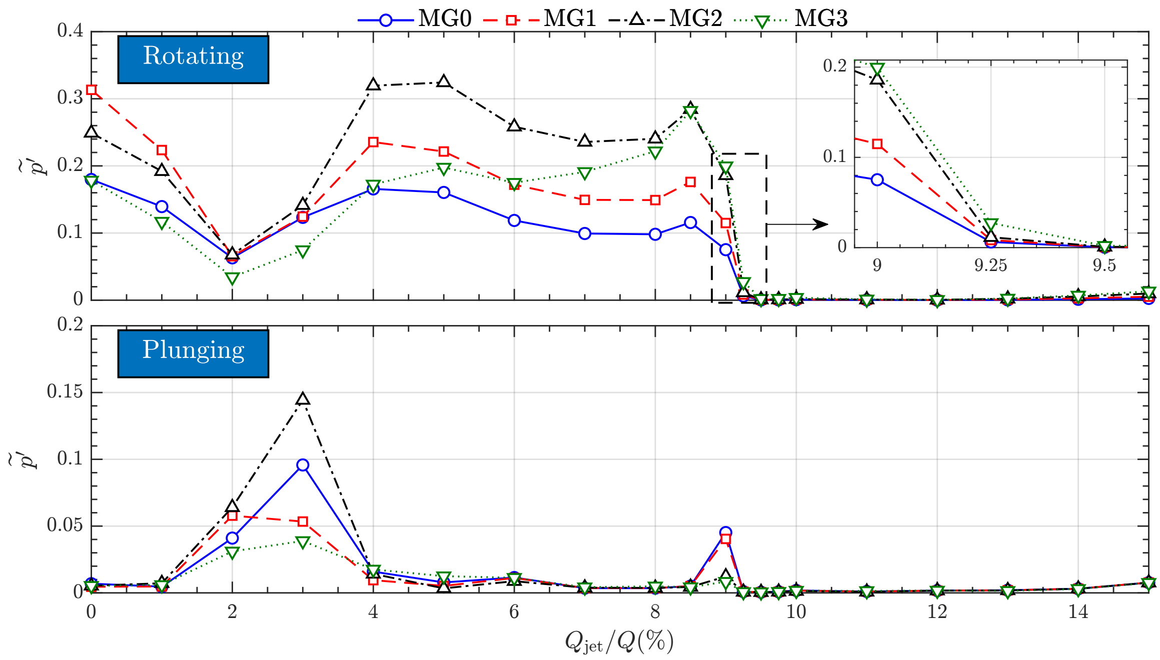

Figure 6: Variation of the amplitudes of rotating and plunging modes with jet flow rate for different pressure locations

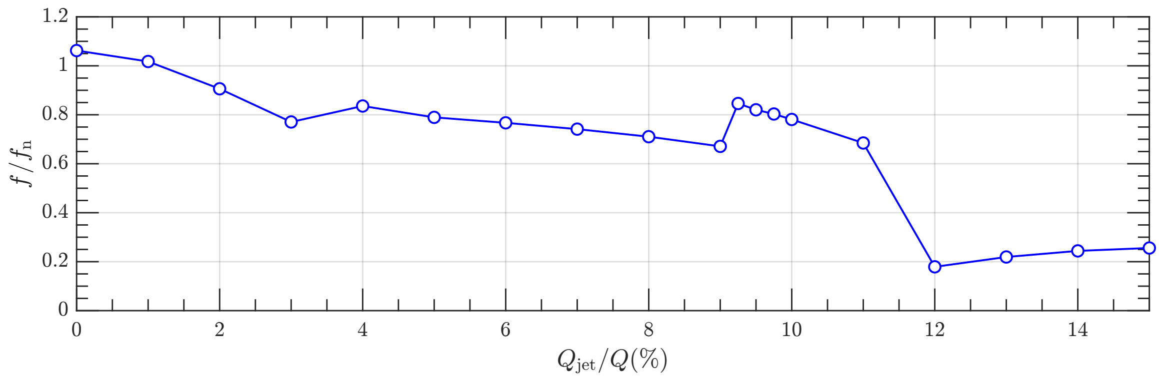

Figure 7: Variation of the fundamental frequency of vortex rope with jet flow rate

critical jet flow rate does not seem to have a significant effect on the plunging mode, and the amplitude shows a consistent gradual decrease.

The fundamental frequency of the vortex rope can be determined by the frequency of the highest amplitude calculated in the FFT of the rotating mode. The variation of the fundamental frequency of the vortex rope with jet flow rate is plotted in Fig. 7. Although the runner was not included in the current computations, its rotational frequency was used for normalization to maintain consistency with our previous studies [6]. The frequency consistently decreases from $f/f_{\mathrm{n}} = 1.07$ at no-jet condition to $f/f_{\mathrm{n}} = 0.66$ at $Q_{\mathrm{jet}}/Q = 9.25\%$. Then, after a slight increase, the frequency decreases with a higher rate to $f/f_{\mathrm{n}} = 0.19$ at $Q_{\mathrm{jet}}/Q = 12\%$. As explained earlier, the vortex rope completely diminishes after the critical jet flow rate $Q_{\mathrm{jet,cr}}/Q = 9.5\%$, and thereby the frequencies observed after this critical threshold are most likely related to the instabilities of the shear layer between the jet and bulk flow.

A frequency analysis was performed on the force components acting on the test section walls

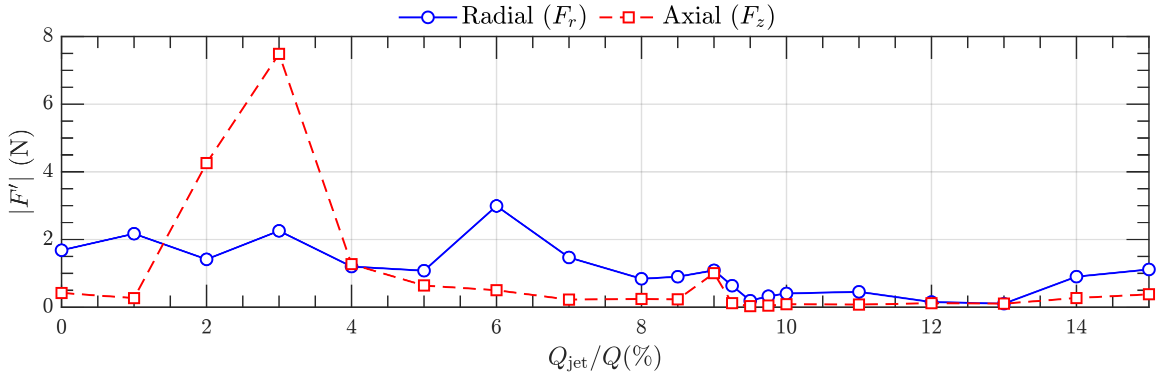

Figure 8: Variation of the amplitudes of radial and axial force components with jet flow rate

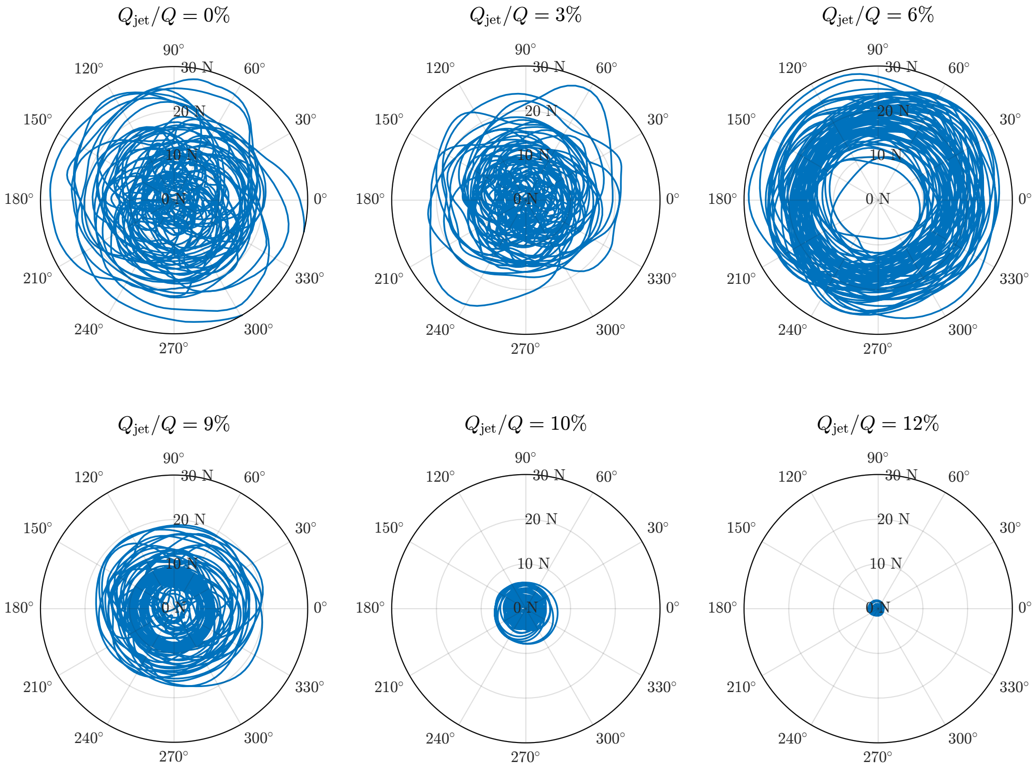

Figure 9: Time variation of magnitude and direction of radial force for different jet flow rates

to investigate the effect of the control mechanism on the forces. Fig. 8 represents the highest amplitude of radial (vectorial sum of the two horizontal components F_x and F_y) and axial (F_z) forces acting on the domain walls at different jet flow rates. As expected, the evolution of the radial force amplitude with jet flow rate is rather similar to the amplitude of the rotating mode in Fig. 6. It increases up to $Q_{\mathrm{jet}}/Q = 6\%$ and then decreases. Similarly, the axial force follows a pattern akin to the plunging effect, since the plunging mode is associated with the axial oscillations of the vortex rope. The axial force experiences a sharp increase at $Q_{\mathrm{jet}}/Q = 3\%$ and then abruptly decreases with further increasing jet flow rate.

The time variation of the magnitude and direction of the radial force for different jet flow rates is illustrated in Fig. 9. The vortex rope precession predominantly drives the changes in the direction of the radial force. It is observed that the magnitude of this component peaks at

$Q_{\text{jet}}/Q = 6\%$ and then decreases. Beyond $Q_{\text{jet}}/Q = 10\%$, the radial force approaches zero with no significant oscillations.

The instantaneous flow field is visualized using the λ_2 vortex identification technique [16] to get deeper insights into the physics of the jet flow control mechanism. Fig. 10 displays the iso-surface of λ_2 criterion as a red surface, whereas, the stagnant region is also illustrated by the zero instantaneous axial velocity ($U_z = 0$) as a blue surface. A strong vortex rope is observed at the no-jet condition. As reported in previous studies [8], the vortex rope helically wraps around the central stagnant region.

Under no-jet conditions, the stagnant region and vortex rope extend up to the runner hub. Increasing the jet flow rate shifts both structures downstream. At $Q_{\text{jet}}/Q = 3\%$, the stagnant region is clearly formed further downstream of the hub. A helical structure remains visible with further increases in Q_{jet}/Q up to 9%, beyond which no precession effect is observed, and the red structure primarily illustrates the shear layer between the jet and the bulk flow. This observation aligns with our previous identification of a critical jet flow rate at $Q_{\text{jet}}/Q = 9.25\%$. However, a large stagnant region remains visible further downstream up to $Q_{\text{jet}}/Q = 11\%$, after which the stagnant region disappears. Increasing the jet flow rate beyond $Q_{\text{jet}}/Q = 11\%$ induces instability in the jet shear layer in the form of Kelvin-Helmholtz instability, which may explain the slight increase in the radial force observed beyond a jet flow rate of 12% in Fig. 8.

The effect of jet flow rate on the stagnant region is further analyzed by examining the time-averaged stagnant region, as shown by the contour line of zero time-averaged axial velocity ($\overline{U_z} = 0$) in Fig. 11. The time-averaged stagnant region gradually moves downstream and elongates by increasing the jet flow rate. It remains nearly symmetrical until $Q_{\text{jet}}/Q = 11\%$, at which the stagnant region is entirely unstable and asymmetrical. No time-averaged stagnant region was observed beyond this jet flow rate.

5. Summary and Conclusion

This study performed an in-depth investigation of the impact of axial flow jets on the mitigation of vortex rope instabilities in hydraulic turbines, particularly under Part Load (PL) conditions. Using the Timisoara Swirl Generator (TSG) model and performing numerical simulations with OpenFOAM, a parametric analysis of axial water injection through the runner hub was conducted.

The results indicate that increasing the jet flow rate effectively enhances pressure recovery. The amplitude of the rotating mode gradually increases with the jet flow rate due to the displacement of the stagnant region downstream. However, after the critical jet flow rate identified at $Q_{\text{jet,cr}}/Q = 9.25\%$, the amplitude drastically reduces and approaches zero. The plunging mode associated with axial oscillations of the vortex rope initially increases considerably with Q_{jet}, and then gradually decreases and diminishes with a further increase in jet flow rate. Additionally, the fundamental frequency of the vortex rope also consistently decreases with the jet flow rate.

The increase in axial jet injection detaches the vortex rope and stagnant region from the runner hub and gradually moves them downstream. The stagnant region appears to be completely removed beyond $Q/_{\text{jet}}/Q = 11\%$.

These findings underscore the potential of axial flow jets as an active flow control strategy to mitigate self-induced instabilities in hydraulic turbines. The study provides insights into the design and optimization of such strategies. Future work will focus on refining these control strategies and exploring and optimizing time-varying controlling mechanisms.

6. Acknowledgements

The research presented was carried out as a part of the “Swedish Centre for Sustainable Hydropower - SVC”. SVC has been established by the Swedish Energy Agency, Energiforsk

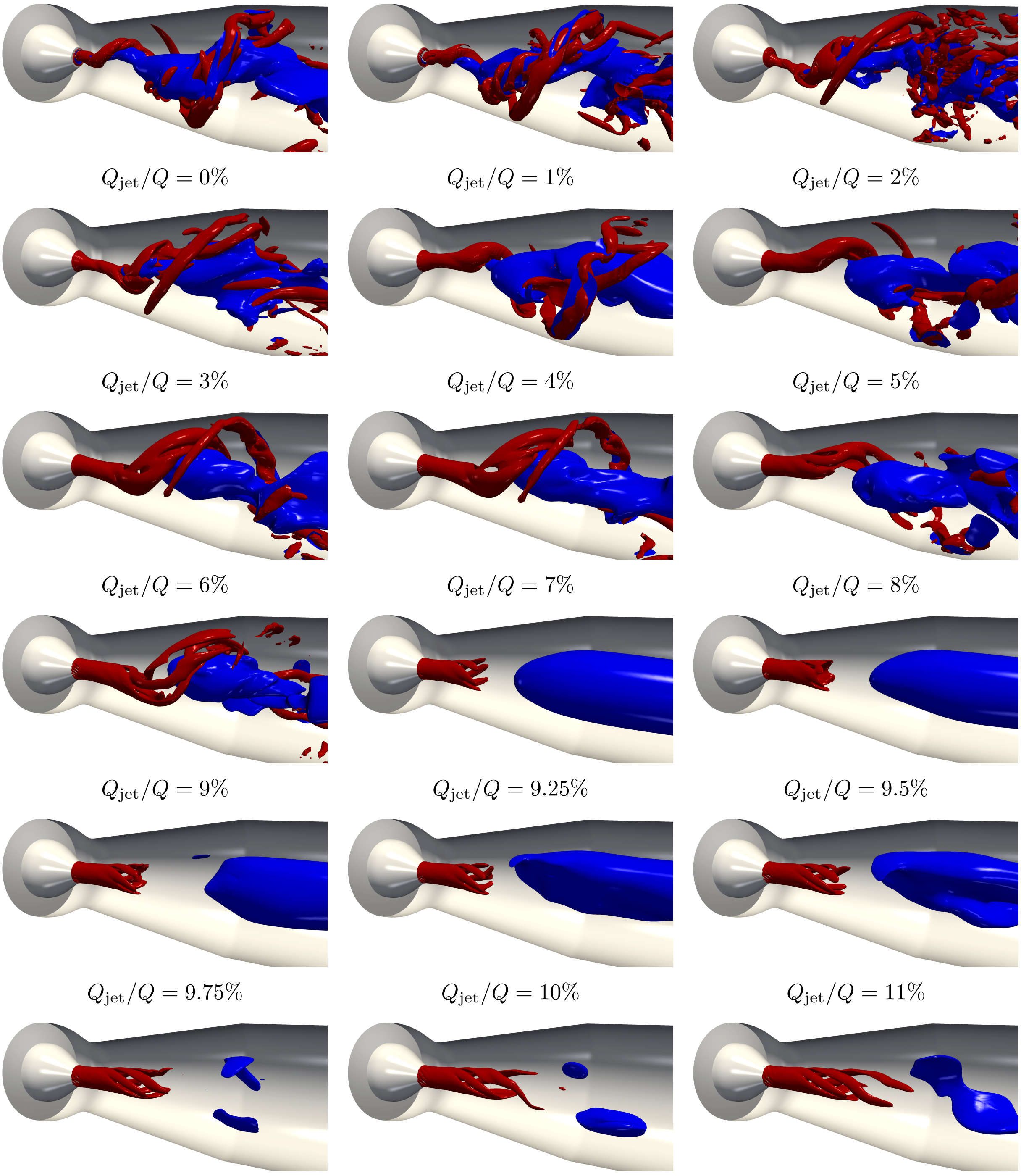

$Q_{\mathrm{jet}}/Q = 0\%$ $Q_{\mathrm{jet}}/Q = 1\%$ $Q_{\mathrm{jet}}/Q = 2\%$

$Q_{\mathrm{jet}}/Q = 3\%$ $Q_{\mathrm{jet}}/Q = 4\%$ $Q_{\mathrm{jet}}/Q = 5\%$

$Q_{\mathrm{jet}}/Q = 6\%$ $Q_{\mathrm{jet}}/Q = 7\%$ $Q_{\mathrm{jet}}/Q = 8\%$

$Q_{\mathrm{jet}}/Q = 9\%$ $Q_{\mathrm{jet}}/Q = 9.25\%$ $Q_{\mathrm{jet}}/Q = 9.5\%$

$Q_{\mathrm{jet}}/Q = 9.75\%$ $Q_{\mathrm{jet}}/Q = 10\%$ $Q_{\mathrm{jet}}/Q = 11\%$

$Q_{\mathrm{jet}}/Q = 12\%$ $Q_{\mathrm{jet}}/Q = 13\%$ $Q_{\mathrm{jet}}/Q = 14\%$

Figure 10: Illustration of the evolution of the vortical flow structures with increasing jet flow rates through iso-surface of $\lambda_2 = 25000\ \mathrm{s}^{-2}$ (the red surface). The blue surface shows the stagnant region represented by the zero instantaneous axial velocity ($U_z = 0$).

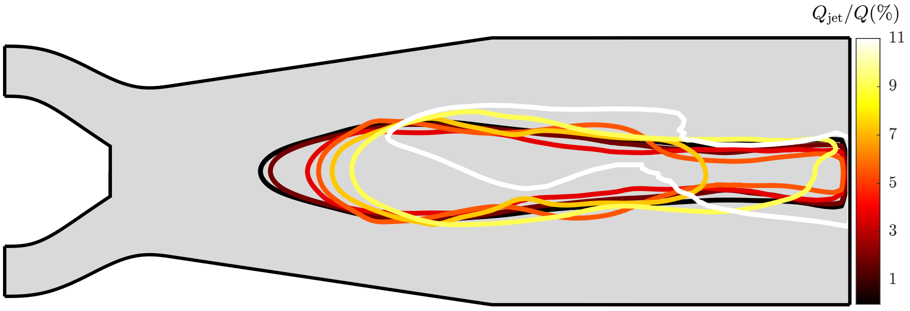

Figure 11: Evolution of time-averaged stagnant region with increasing jet flow rate. The region is represented by the contour line of zero time-averaged axial velocity ($\overline{U_z} = 0$). No separation zone was observed for $Q_{\text{jet}}/Q > 11\%$.

and Svenska kraftnät together with Luleå University of Technology, Uppsala University, KTH Royal Institute of Technology, Chalmers University of Technology, Karlstad University, Umeå University, and Lund University.

The computations were enabled by resources provided by the National Academic Infrastructure for Supercomputing in Sweden (NAISS) at NSC and C3SE partially funded by the Swedish Research Council through grant agreement no. 2022-06725.

References

[1] Goyal R and Gandhi B K 2018 *Renewable Energy* **116** 697–709 ISSN 0960-1481
[2] Liu X, Luo Y and Wang Z 2016 *Renewable and Sustainable Energy Reviews* **54** 1–14 ISSN 1364-0321
[3] Susan-Resiga R, Vu T C, Muntean S, Ciocan G D and Nennemann B 2006 Jet control of the draft tube vortex rope in francis turbines at partial discharge *23rd IAHR Symposium Conference* pp 67–80
[4] Susan-Resiga R and Muntean S 2009 Decelerated swirling flow control in the discharge cone of Francis turbines *Fluid Machinery and Fluid Mechanics* ed Xu J, Wu Y, Zhang Y and Zhang J (Berlin, Heidelberg: Springer Berlin Heidelberg) pp 89–96
[5] Bosioc A I, Susan-Resiga R, Muntean S and Tanasa C 2012 *Journal of Fluids Engineering* **134** ISSN 0098-2202 081104
[6] Salehi S and Nilsson H 2024 *Physics of Fluids* **36** 024122 ISSN 1070-6631
[7] Egorov Y and Menter F 2008 Development and application of SST-SAS turbulence model in the DESIDER project *Advances in Hybrid RANS-LES Modelling* ed Peng S H and Haase W (Berlin, Heidelberg: Springer Berlin Heidelberg) pp 261–270
[8] Salehi S, Nilsson H, Lillberg E and Edh N 2021 *Renewable Energy* **179** 2322–2347 ISSN 0960-1481
[9] Salehi S and Nilsson H 2022 *Renewable Energy* **188** 1166–1183 ISSN 0960-1481
[10] Salehi S and Nilsson H 2023 *Computer Physics Communications* **287** 108703 ISSN 0010-4655
[11] Masoodi F A, Salehi S and Goyal R 2024 *Physics of Fluids* **36** 025116 ISSN 1070-6631
[12] Weller H G, Tabor G, Jasak H and Fureby C 1998 *Computers in Physics* **12** 620–
[13] OpenCFD 2023 *OpenFOAM - The Open Source CFD Toolbox - User's Guide, Version v2306* OpenCFD Ltd.
[14] Weller H 2012 *Monthly Weather Review* **140** 3220–3234 ISSN 0027-0644
[15] Muntean S, Nilsson H and Susan-Resiga R F 2009 3D numerical analysis of the unsteady turbulent swirling flow in a conical diffuser using Fluent and OpenFOAM *Proceedings of the 3rd IAHR International Meeting of the Workgroup on Cavitation and Dynamic Problem in Hydraulic Machinery and Systems, Brno, Czech Republic*
[16] Jeong J and Hussain F 1995 *Journal of Fluid Mechanics* **285** 69–94